Nonadiabaticity in the iron bcc to hcp phase transformation

Donald F. Johnson[1] and Emily A. Carter[2,a)]

[1]*Department of Chemistry, Princeton University, Princeton, New Jersey 08544, USA*
[2]*Department of Mechanical and Aerospace Engineering and Program in Applied and Computational Mathematics, Princeton University, Princeton, New Jersey 08544-5263, USA*

Iron is known to undergo a pressure-induced phase transition from the ferromagnetic (FM) body-centered-cubic (bcc) α-phase to the nonmagnetic (NM) hexagonal-close-packed (hcp) ε-phase, with a large observed pressure hysteresis whose origin is still a matter of debate. Long ago, Burgers [Physica (Amsterdam) **1**, 561 (1934)] proposed an adiabatic pathway for bcc to hcp transitions involving crystal shear followed by atom shuffles. However, a quantum mechanics search in six-dimensional stress-strain space reveals a much lower energy path, where the crystal smoothly shears along the entire path while the atoms shuffle only near the transition state (TS). The energy profile for this phase transition path exhibits a cusp at the TS and closely follows bcc and hcp diabatic energy wells. Both the cusp and the overlap with diabatic energy surfaces are hallmarks of nonadiabaticity, analogous to, e.g., electron transfer (ET) reactions in liquids. Fluctuations in the positions of FM bcc iron atoms near the TS induce magnetic quenching (akin to solvent fluctuations inducing ET), which then promotes NM hcp iron formation (akin to solvent reorganization after ET). We propose that the nonadiabatic nature of this transition at the atomic scale may contribute to the observed pressure hysteresis. © *2008 American Institute of Physics*. [DOI: 10.1063/1.2883592]

INTRODUCTION

Solid state phase transitions are important to materials processing and have been exploited for centuries in steel production and more recently with shape-memory alloys, e.g., in medical applications such as stents. Cooling rates in steel processing limit the length scales on which atoms can diffuse, which consequently determines the microstructure of the resultant phases. The microstructure in turn affects bulk properties such as strength, ductility, and toughness. Phase transitions are typically classified into two types: those involving diffusion of atoms and those consisting of cooperative short-range atomic movements. In diffusion-dependent transitions, such as a eutectic transition, a single phase alloy forms two separate phases with different compositions. However, when a material is shocked or cooled rapidly, the atoms do not have time to diffuse long distances and a martensitic transformation takes place (named in honor of Martens, who first studied in detail this type of transition in steel).[1] In both cases, new phases are thought to nucleate and then grow, either on the atomic length scale as atoms diffuse or on longer length scales in the case of martensitic transitions. In diffusionless martensitic transformations, large numbers of atoms undergo coordinated movements. The strict geometrical constraints imposed by the crystal plane relationships give the resultant martensitic crystal a rich microstructure with fine-scale stacking faults (e.g., slip and twinning planes). Despite great technological importance, much about martensitic phase transformations is yet to be understood.

One can view most phase transformations as smooth transitions between minima on an energy landscape, similar to how chemists view adiabatic chemical reactions, where one energy well represents reactants, the other products. In chemistry, one also encounters nonadiabatic reactions, the most ubiquitous of which is the electron transfer reaction. Here, the well-known Marcus picture applies,[2] in which two diabatic states—the solute+solvent states prior to and after electron transfer—have intersecting parabolic free energy curves. Fluctuations in the surrounding solvent molecules can produce a state where the new charge configuration is energetically favorable. Once solvent fluctuations and solute molecular vibrations have brought the system to the crossing point of the parabolic wells (the transition state), charge transfer is fast and the system relaxes to reflect the new charge distribution. Solid state phase transformations are often assumed to follow smooth, adiabatic pathways. We illustrate below that this is not always the case and, in particular, that the lowest energy pathway for the pressure-induced bcc to hcp transition in Fe exhibits precisely this curve-crossing behavior: fluctuations in atomic positions cause a sudden change in the electronic structure (a loss of magnetism), which then makes it favorable to form the nonmagnetic (NM) hcp phase of Fe. Hence, in this work, we propose that the concept of nonadiabatic processes can be extended to the realm of solid state phase transformations. Before proceeding to our findings, we briefly review what is known about the transformation of interest here, namely, the Fe bcc to hcp phase transition.

Under high pressure or shock conditions, Fe undergoes a martensitic phase transition from the bcc α-phase to the hcp ε-phase,[3] as evidenced by formation of laminate microstructures.[4,5] The $\sim$13 GPa transformation[6,7] exhibits significant pressure hysteresis (width of $\sim$5 GPa), with a wide range of measured bcc to hcp transition pressures

(9–20 GPa).[8–10] Mesoscale processes such as nucleation of crystallites and dislocation motion are acknowledged contributors to the observed hysteresis,[11] but the current work indicates that atomic scale mechanisms also may contribute. Recent quantum-based multiscale simulations[12,13] offered possible explanations for both the range of transition pressures and the hysteresis, where the former was suggested to be due to a variety of shear states present in the experiments while a contributing factor to the latter was kinematic constraints on the allowed microstructures that could form. However, this simulation did not consider the contribution of atomic scale mechanisms, which is the focus of the present work.

Despite any innate differences, many materials exhibiting a bcc to hcp transition are assumed to follow the Burgers path.[14] Indeed, Fe was proposed to follow a virtually identical pathway when the bcc to hcp transition was discovered in Fe by Mao *et al.* in 1967 (Ref. 15) and is still commonly referred to as the Burgers path. In this path, the crystal undergoes shear deformation and shuffling of atomic planes; the simple assumption made by Burgers was that these two steps are decoupled and sequential. Although the atomic scale mechanism has not yet been determined by experiment, extended x-ray absorption fine structure measurements[16] and simultaneous x-ray magnetic circular dichroism/absorption spectroscopy[17,18] have revealed important features of the mechanism: quenching of magnetism is directly correlated with the structural transition, which is extremely sharp and is first order (discontinuous) in nature. Recent *in situ* x-ray diffraction measurements of the shock-driven Fe transition[19] observed compression (in the shock direction) of the bcc lattice followed by phase transformation to hcp, proving that the transition also occurs under dynamic shock loading. Apart from the relationships between the initial bcc lattice planes and final hcp lattice planes, real-time measurements have been unable to precisely probe the atomic-scale mechanism, although the recent development of ultrafast electron microscopy[20] may make this possible in the future.

Theoretical investigations into the phase transition have been more extensive. Molecular dynamics (MD) simulations of shocked Fe using embedded atom method potentials predicted formation of a split wave front (elastic followed by phase transition front) and picosecond scale grain growth,[21] which was later confirmed experimentally.[19] More recent MD simulations[22] of shocked Fe suggested that, in addition to hcp Fe formation, metastable face-centered-cubic Fe may form within the first few picoseconds, which then might relax to hcp and hence not be observable in the nanosecond scale *in situ* experiments. Tight-binding[23] and density functional theory[24–28] (DFT) calculations employing the generalized gradient approximation (GGA) for electron exchange-correlation mainly have investigated crystal structure phase stability. The most extensive DFT-GGA study[29] mapped out two-dimensional (Burgers' shear and shuffle) energy surfaces at several volumes and an enthalpy surface at their predicted transition pressure. The cusp on the minimum energy surface described below was also found on these constant volume and constant pressure surfaces and was also observed to be correlated with the loss of magnetism.[29]

The objective of the current investigation is to find the minimum energy pathway (MEP) for conversion of bcc to hcp Fe at the atomic scale, without *a priori* assumption of the Burgers or any other reaction coordinate and by conducting the search in the full dimensional deformation space (six degrees of freedom, due to the invariance of the energy to rigid body rotations), which has not been attempted before. We demonstrate that the Burgers' path of shear followed by atomic shuffle is too simplistic and high energy, while a recently proposed scheme that minimizes stress along the pathway (discussed below) yields unphysical results. We identify a much lower energy path that contains an energy cusp similar to the one identified along the Burgers coordinates earlier.[29] Such a cusp is characteristic of a first-order phase transformation. We go on to show that the energy profile maps nearly exactly onto a superposition of diabatic ferromagnetic (FM) bcc and NM hcp energy wells, allowing us to draw a new connection between structural/magnetic phase transitions in solids and nonadiabatic processes in chemistry. This analogy further allows us to gain new insight into the observed pressure hysteresis by recognizing the need for an atomic reorganization before electronic (in this case, spin) reorganization can occur.

THEORY

A robust transition state search algorithm, such as the nudged elastic band (NEB) method,[30] may be best suited to identify the MEP, though in the present case, both atomic motion and cell shape must be considered simultaneously. While MD methods exist that allow cell volume to vary along with atomic motion,[31–33] they require *a priori* assumption of the most important collective coordinates including a reaction coordinate. By contrast, the NEB approach *predicts* the reaction coordinate, simply given knowledge of the initial and final states.

When applying the NEB method to a solid state transformation, one can imagine two limiting cases: atomic motion driving lattice deformation or bulk deformation driving atomic motion. The first scheme, the atomically driven NEB (A-NEB), developed by Jónsson *et al.*[30] and Henkelman *et al.*[34] for chemical reactions, finds a saddle point search in force-position space. Trinkle *et al.* applied the A-NEB to examine phase transformations in Ti,[35] where they minimized stress by finding optimal lattice vectors along the path simultaneous with optimizing a MEP for the atomic motion. The second scheme, the solid state nudged elastic band (SS-NEB) method developed by Caspersen and Carter,[36] conducts a saddle point search in stress-strain space, with atomic relaxation along the path and where the stress is zero only at the saddle point. In the SSNEB, a Born–Oppenheimer-type approximation is assumed, where atomic motion proceeds on a faster time scale than bulk deformation and minimum energy atomic configurations are found for each lattice deformation along the phase transformation path. This approximation is meant to mimic conditions in slowly pressurized samples, such as in diamond anvil experiments.[16] Given that the Fe martensitic transformation is pressure driven, the SS-NEB, with lattice deformation as the driver, should provide a

better description of the pathway. In this work, we analyze and compare the Fe bcc to hcp transition along the Burgers path and along the two limiting cases of NEB pathways. We now discuss these pathways in more detail.

In constructing the three pathways, we assume a strict two-step linear interpolation for the Burgers path with no relaxation, while the two NEB pathways are initialized as linear interpolations and then allowed to relax according to their individual scheme. Images (interpolated structures) are constructed between the initial and final states, where each image is described by a metric tensor $\mathbf{h}$ (whose columns are the lattice vectors) and atomic positions $\mathbf{r}_1$ and $\mathbf{r}_2$ of the two unique Fe atoms in the unit cell. The transition is best represented[36] by a two-atom hexagonal cell which takes the bcc lattice vectors,

$$\mathbf{h}_{\text{bcc}} = \frac{a_0}{2} \begin{pmatrix} 2 & 1 & 0 \\ 0 & \sqrt{2} & 0 \\ 0 & 0 & 2\sqrt{2} \end{pmatrix},$$

to the hcp lattice vectors,

$$\mathbf{h}_{\text{hcp}} = \frac{a_0 \gamma}{4} \begin{pmatrix} 2\sqrt{3} & \sqrt{3} & 0 \\ 0 & 3 & 0 \\ 0 & 0 & \alpha 4\sqrt{2} \end{pmatrix},$$

by way of the transformation matrix,

$$\mathbf{U}_{\text{bcc}\to\text{hcp}} = \frac{\gamma}{4} \begin{pmatrix} 2\sqrt{3} & 0 & 0 \\ 0 & 3\sqrt{2} & 0 \\ 0 & 0 & 4\alpha \end{pmatrix},$$

where a_0 is the bcc lattice constant, γ controls the density of the hcp phase, and α controls the c/a ratio of the hcp phase. Here, $\gamma = [4\sqrt{6} V_{\text{hcp}} / 9\alpha V_{\text{bcc}}]^{1/3}$ and $\alpha = \sqrt{\frac{3}{8}}(c/a)$, and V_i are the volumes per atom of the hcp and bcc phases. The atomic positions are $\mathbf{r}_1 = (0\ 0\ 0)$ and $\mathbf{r}_2 = (\frac{1}{2}\ 0\ \frac{1}{2})$ in the bcc cell and $\mathbf{r}_1 = (0\ 0\ 0)$ and $\mathbf{r}_2 = (\frac{1}{3}\ \frac{1}{3}\ \frac{1}{2})$ in the hcp cell.

For the Burgers path, we assume a linear interpolation of the lattice deformation from images 1–5 followed by an equal length linear interpolation of the atomic shuffle from images 5–9. Note the "length" of the linear interpolation is arbitrary in this path. The A-NEB was initialized as a linear interpolation of nine images and was relaxed according to the method outlined by Jónsson *et al.*,[30] with stress minimization done upon reaching a minimum energy configuration of the atoms for each image.

The SSNEB pathway was initialized as a linear interpolation from the bcc crystal structure to the hcp crystal structure. Initially, the band consisted of nine images, but after some relaxation, another seven images were strung between images 6 and 8 of the original band. This nine-image band was further relaxed to obtain better resolution around the transition state (TS). Due to the discontinuity near the TS discussed below, the climbing image NEB scheme[34] was not used.

The SSNEB path was optimized using the method outlined by Caspersen and Carter.[36] For each image, we calculate the true stress as

$$\boldsymbol{\sigma}_t = -\Omega(\boldsymbol{\sigma}_{\text{Cauchy}} + \mathbf{P} \cdot \mathbf{I})(\mathbf{h}^{-1})^T, \qquad (1)$$

where Ω is the cell volume, $\mathbf{P}$ is the external pressure, and $\boldsymbol{\sigma}_{\text{Cauchy}}$ is the Cauchy stress tensor: $\Omega^{-1}(dE/d\mathbf{h})\mathbf{h}^T$, where E is the total energy. The spring stress is $\boldsymbol{\sigma}_s = -dE_{\text{spring}}/d\mathbf{h}$, where $E_{\text{spring}} = k_s \sum \boldsymbol{\varepsilon}_i : \boldsymbol{\varepsilon}_i$. The strain $\boldsymbol{\varepsilon}_i$ is the distance between images defined as $\mathbf{h}_{i+1} = (\mathbf{I} + \boldsymbol{\varepsilon}_i)\mathbf{h}_i$ and the value of k_s used is 6.5 eV/Å^2. At each image i, $\boldsymbol{\sigma}_t$ and $\boldsymbol{\sigma}_s$ are projected into perpendicular and parallel components by fitting cubic spline functions to the components of $\mathbf{h}_{i-2}$ to $\mathbf{h}_{i+2}$. The SSNEB reshaping equation for nudging the images is then defined as $\mathbf{h}' = \mathbf{h} + (\sigma_t^\perp + \sigma_s^\parallel)\Delta t$, where Δt is an arbitrary time step. The Cauchy stress tensor is calculated from first-principles DFT and input to Eq. (1) and the cell reshaping equation.

CALCULATIONAL DETAILS

For each band, we calculate the bulk properties of Fe at each image, including total energy, Cauchy stress tensor, and magnetism. The Vienna *ab initio* simulation package[37] was employed using spin-polarized DFT within the PBE GGA (Ref. 38) for electron exchange and correlation. The all-electron (frozen core) projector augmented wave (PAW) method[39,40] was used since it correctly predicts the ordering of structural and magnetic states of Fe, when used in conjunction with the GGA exchange correlation.[41–43] PAW potentials that represent the nuclei plus core electrons up through the $3p$ shell were employed. A kinetic energy cutoff of 500 eV for the plane wave basis set and a $(15 \times 15 \times 15)$ Monkhorst–Pack k-mesh was used, which converged the total energies to 5 meV/atom. Brillouin zone integration was done using the Methfessel–Paxton smearing method[44] using a smearing width of 0.1 eV.

Forces on the nuclei were considered minimized when they were below 10^{-5} eV/Å. The SSNEB is considered minimized when the total nudged force on each image $(|\sigma_t^\perp + \sigma_s^\parallel|)$ is below 0.005 eV/Å. The predicted transition pressures for each path are estimated from the diagonal elements of the stress tensor calculated at the highest energy bcc-like image (prior to phase transformation) of that path. Since the system is in mechanical equilibrium prior to the phase transformation, the internal pressure we calculate from the stress tensor is equal to the external pressure that would be required to achieve that state of deformation.

Magnetic moments were calculated by integrating the charge density throughout the entire cell for each spin component and averaging the difference $(\alpha - \beta)$ over the number of atoms in the cell (two). Spin-polarized calculations were performed for both phases, leading to a FM ground state for bcc Fe and relaxation of an antiferromagnetic (AF) initial guess (AFI, with AF coupling between basal planes) to a NM ground state for hcp Fe. Other all-electron DFT-GGA calculations have proposed an AFII ground state (involving AF coupling between planes perpendicular to the hcp basal planes).[45,46] However, the maximum energy difference between NM and AFII for all distortions considered was ~0.03 eV/atom, which is within expected error bars of the GGA model. Over the volume range reached during the transition path, we find both AF states to be degenerate with the NM state to within <0.02 eV/atom. Conflicting interpreta-
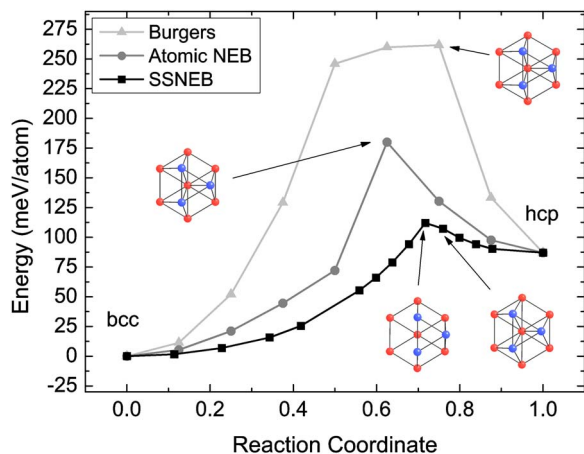
FIG. 1. (Color online) Energy profiles for the SSNEB (squares), the atomically driven (minimum stress) NEB (circles), and the Burgers (triangles) pathways. The predicted energy barriers are 112, 225, and 260 meV, respectively. The insets show projections of the atoms in two (110) planes of Fe.

tions of various experiments have not resolved this controversy: Mössbauer measurements exhibit no sign of hyperfine interactions expected for a magnetic state,[47,48] while Raman[49] and superconductivity[50,51] measurements indirectly imply possible presence of local moments. Importantly, we find "AFMII hcp Fe" to be unstable with respect to breaking structural symmetry: this spin coupling drives the system away from a hexagonal structure. The only stable hcp structure that maintains the observed hcp structural symmetry is the NM state; we therefore modeled hcp Fe as NM, as previous authors have also done.[29] Even if AFMII turns out to be the actual "hcp-like" ground state, it would not affect our findings and conclusions given below.

RESULTS AND DISCUSSION

Each of the three iron bcc to hcp phase transformation pathways was analyzed in detail by charting bulk properties and structural features. Figure 1 compares the phase transition energy profiles for all three pathways. The energy barriers for the Burgers, the A-NEB, and the SSNEB pathways are estimated to be 260, 180, and 112 meV/atom. The Burgers pathway shows a sharp rise in energy during the cell deformation with a broad peak corresponding to the atomic shuffle. By contrast, the A-NEB displays a sharp peak midway through the transition. The SSNEB path has a cusp at the transition state, but has the lowest energy barrier. The SSNEB barrier is in line with the barrier of 122 meV/atom found earlier on a constant volume two-dimensional energy surface.[29]

As discussed above, the measured transition pressure is ~13 GPa,[6,7] but reports range between 9 and 20 GPa.[9,10,52] For the energy curves with zero external pressure (Fig. 1), the estimated transition pressures for the Burgers, A-NEB, and SSNEB paths are 31, 0, and 16 GPa, respectively. The A-NEB scheme minimizes stress at each point along the path, thus the pressure is zero everywhere along the A-NEB path. This unphysical outcome exposes the flaws of the A-NEB scheme in capturing the details of a pressure-induced transformation. The SSNEB scheme, which finds a minimum
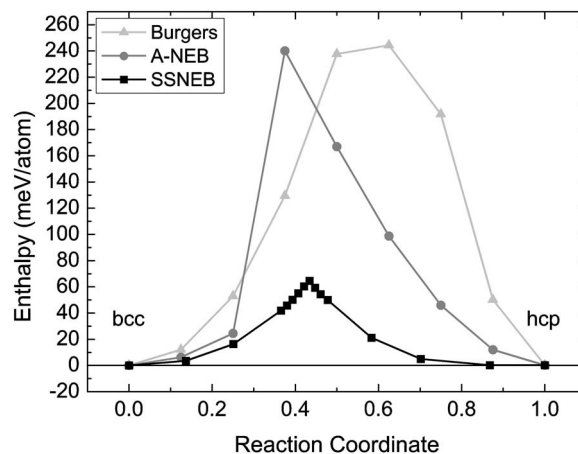
energy path in stress-strain space (including nonhydrostatic stresses along the path), yields the transition pressure in closest agreement with experiment.

The three band methods were also run with an external pressure of 13.1 GPa, the pressure at which we find the bcc and hcp phases to have equal enthalpies, which is similar to an isoenthalpic pressure of 10.3 GPa predicted previously.[29] This pressure of 13.1 GPa may be considered a lower bound on the transition pressure; note that this value is consistent with our earlier estimate of the SSNEB transition pressure of 16 GPa. The enthalpy was calculated for each image as $H = E + PV$, where P is the external pressure applied according to Eq. (1) and E and V are the energy and volume of the particular image. The resulting enthalpy curves (Fig. 2) again show a much lower barrier for the SSNEB pathway (65 meV/atom) compared to the Burgers and A-NEB pathways (~240 meV/atom). The SSNEB barrier is slightly lower than a 109 meV/atom enthalpy barrier predicted by Ekman et al.,[29] suggesting the SSNEB path to be the most favorable. Comparing the enthalpy curves of just the SSNEB path at three different pressures (Fig. 3) shows that the enthalpy barrier of the transition decreases with increasing ex-

FIG. 2. Enthalpy profiles for SSNEB (squares), A-NEB (circles), and the Burgers (triangles) pathways under an external pressure of 13.1 GPa.
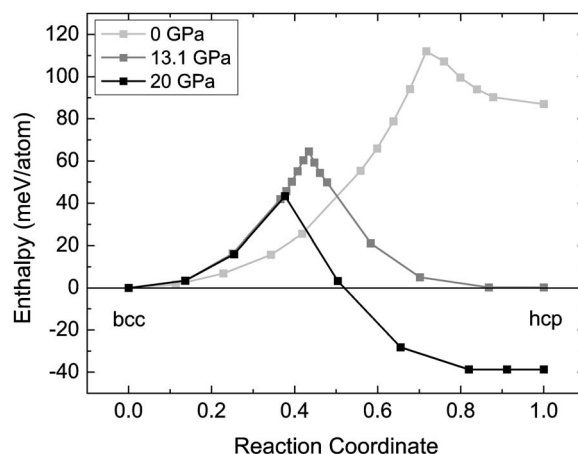

FIG. 3. Comparison of SSNEB enthalpy profiles at varying external pressures: 0 GPa (light gray), 13.1 GPa (gray), and 20 GPa (black). The bcc and hcp states have equal enthalpy at 13.1 GPa.
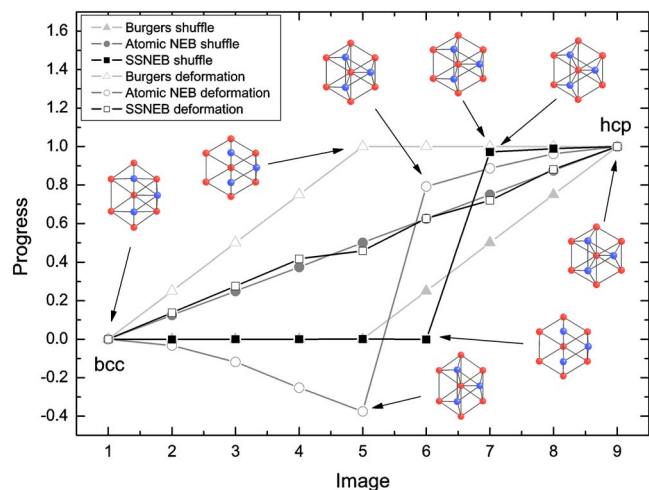
FIG. 4. (Color online) Comparison of phase transition mechanisms. The extent of the transition is plotted at each image for the SSNEB (squares), atomic NEB (circles), and Burgers path (triangles). Open symbols represent the progress of the lattice deformation and filled symbols represent atomic shuffle progress. The inset pictures show a projection of the atoms in two (110) planes of Fe.

FIG. 5. The magnetic moment per Fe atom in the SSNEB transformation path. The loss of magnetism accompanies the atomic shuffle from bcc to hcp.

ternal pressure, as expected. The same cusp behavior seen in the energy profiles also occurs in the SSNEB enthalpy profiles at all three pressures.

To further characterize the different phase transition mechanisms, we separate cell deformation from atomic shuffle and plot the resulting transition progress at each image in Fig. 4. We define the progress of $\vec{x}$ at image i as $P(\vec{x}) = (\vec{x}_i - \vec{x}_{bcc}) \cdot (\vec{x}_{hcp} - \vec{x}_{bcc}) / \|\vec{x}_{hcp} - \vec{x}_{bcc}\|$, where the deformation progress is given by the average progress of the three lattice vectors: $\frac{1}{3}(P(\vec{a}) + P(\vec{b}) + P(\vec{c}))$ and the shuffle progress is defined as $P(\vec{d})$, where $\vec{d} = \vec{r}_2 - \vec{r}_1$ the distance between the two atoms in the unit cell in fractional coordinates. In the Burgers path, during the first half of the transition, the crystal cell deforms, while no progress is made for the atomic shuffle. In the second half of the transition, the atoms shuffle from bcc to hcp while the crystal cell remains fixed to the hcp lattice vectors. An arbitrary choice was made to separate the shear and shuffle into equal halves, but the weight given to each step does not affect the analysis. The Burgers path TS (point of highest energy, Fig. 1) appears midway through the atomic shuffle. In the A-NEB, the atoms smoothly shuffle from the bcc to the hcp configuration, while the cell deformation is more abrupt. To accommodate the large stresses induced by the shuffling atoms, the cell initially expands, which is shown as "negative" progress in Fig. 4. In the A-NEB, the energy peaks (Fig. 1) where the atoms are in an intermediate state, similar to the Burgers path, but this peak is accompanied by a sharp change in the bulk crystal shape. In the SSNEB path, deformation occurs rather smoothly, while the atoms make a sharp jump at the TS, from the bcc to the hcp configuration. Lattice constant changes are small and smooth along the entire SSNEB path. The volume along the SSNEB path decreases by 6.64% going from the equilibrium bcc phase to the TS and then by another 3.84% from the TS to the equilibrium hcp phase for an overall shrinkage of 10.48% relative to the equilibrium bcc volume.
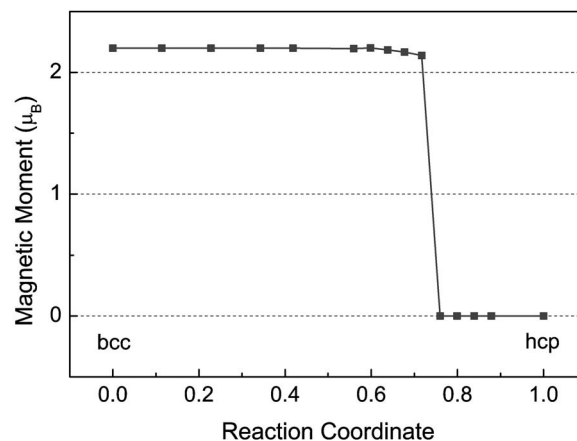
Comparing Figs. 1 and 4 reveals that the highest energy image in the SSNEB pathway is in a bcc configuration, while the next image is in a mainly hcp configuration. The deformation is smooth with an abrupt shuffle, and the energy peaks in a cusp around this atomic shuffle. To test whether the energy cusp is simply due to the abrupt atomic movement, we mapped out the energy profile when the atoms are forced to move smoothly between the two highest energy SSNEB images via an unrelaxed interpolation. Even in this case, the energy cusp remained. One may wonder if the cusp is an artifact of the SSNEB algorithm, in which we assume that deformation drives atoms to their minimum energy configurations at each stage of deformation. However, in earlier work exploring the bcc to hcp transition in Li,[36] we showed that the SSNEB method gives rise to no such cusp and in fact to a smooth adiabatic pathway with a normal saddle point. The difference between Fe and Li is clear: in Li, no electronic transition (change in magnetism) occurs, whereas in Fe, a change in magnetism accompanies this transition. Therefore, the SSNEB algorithm has proven itself capable of finding smooth pathways where they exist physically. For Fe, this is simply not the case due to its magnetic complexity, as we discuss next.

We observe that the atomic shuffle at the TS of the SSNEB path is accompanied by a loss of magnetism, as shown in Fig. 5. Just before the TS, while in bcc configuration, the magnetic moment on each atom is very close to that of the equilibrium α-Fe ground state: $2.2\mu_B$. The atomic magnetic moment drops to 0 when the atoms shuffle to the hcp configuration. This magnetic quenching was also noted in the two-dimensional Burgers coordinates explorations by Ekman et al.[29] The loss of magnetism under compression makes sense: as the FM Fe atoms get closer, Pauli exchange repulsion between FM Fe electrons will favor spin flipping to quench the magnetism and the exchange repulsion. These trends are consistent with x-ray magnetic circular dichroism experiments that found the magnetic moment to be closely correlated with the bcc/hcp phase fraction.[18]

The minimum energy SSNEB pathway exhibits the same type of cusp found earlier in two-dimensional Burgers coordinate maps,[29] but in addition, we noticed that the energy
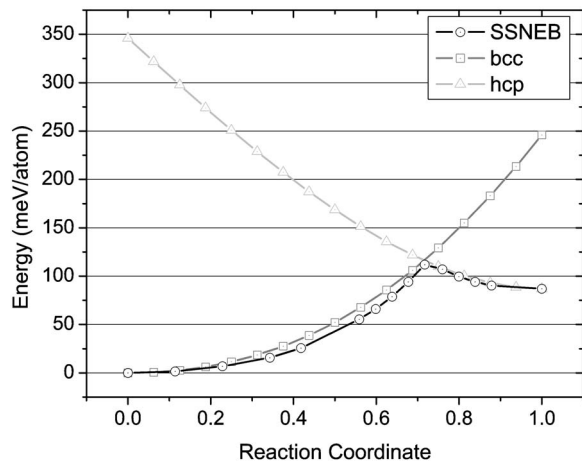
FIG. 6. Energy profile of the SSNEB (black circles) phase transition pathway compared with diabatic energy profiles of bcc Fe (gray squares) and hcp Fe (light gray triangles) atomic configurations subjected to linear interpolation of lattice vectors between bcc and hcp Fe.

profile closely follows diabatic equations of state for bcc and hcp Fe (Fig. 6). These diabatic curves were constructed by constraining the atomic positions to remain in the bcc (hcp) configuration and then linearly interpolating the lattice vectors from α to ε, producing the dark gray bcc (light gray hcp) curve in Fig. 6. The electronic structure was also constrained in the bcc diabatic curve to be FM, while it was constrained to be NM in the hcp diabatic curve. That the SSNEB path lies directly on top or just below these two diabatic equations of state is the hallmark of a nonadiabatic process. Thus, as the Fe crystal is deformed, the atoms remain in a bcc configuration. Once the deformation reaches the TS, atomic vibrations and magnetic fluctuations cause the atoms to move to the hcp configuration. This shuffle will propagate through the crystal and quench the magnetism. After the crystal adopts the hcp structure, further deformation ensues, which brings the Fe crystal along the hcp energy surface to the final equilibrium ε state. The cusped energy profile is consistent with the sharp and discontinuous change in structure and magnetism observed in experiment and interpreted by theory as a first order transition.[18,29] As a first order martensitic phase transition, the discontinuity at the point of magnetic collapse (TS) is expected by symmetry,[53] and similar behavior is seen in other materials where strain and polarization are coupled.[54]

CONCLUSIONS

We have performed all-electron spin-polarized DFT-GGA calculations comparing three possible pathways for the Fe bcc to hcp phase transformation. The recently proposed SSNEB method, which finds a minimum energy path in six-dimensional stress-strain space, produced the lowest energy pathway yet found and a transition pressure in good agreement with experiment. The pathway differs considerably from the longstanding mechanism proposed by Burgers because the new pathway involves smooth shear deformations all along the path with atomic motion limited to just around the transition state.

This lowest energy MEP exhibits all the hallmarks of a nonadiabatic process (a cusp at the TS and an energy profile that essentially is a superposition of diabatic energy curves), which offers a new perspective on solid state phase transitions. Drawing analogies to nonadiabatic electron transfer processes in liquids[55–57] makes sense when one considers the loss of magnetism that accompanies the transition. Just as fluctuations in the surrounding solvent molecules allow a solute molecule to undergo a charge transfer, so do atomic position fluctuations in a solid under compression allow magnetism to be quenched to eliminate Pauli exchange repulsion and allow a solid state phase transition in pressurized Fe to occur. This nonadiabatic view of the bcc to hcp phase transition in Fe may also help explain the observed pressure hysteresis, in which there is a lag in the transition pressure for hcp to return to bcc. The reverse transformation requires a rare atomic fluctuation in nonmagnetic hcp Fe to drive the NM state to align spins into the FM state. As hcp Fe is allowed to decompress, it may take longer to find that fluctuation for which it is favorable to align the spins and form FM bcc Fe, akin to the role of solvent friction in electron transfer in liquids. It would be interesting to examine whether an externally applied magnetic field delays the onset of the transition in a diamond anvil experiment by stabilizing the FM bcc phase; here, the applied magnetic field would provide the analogue of solvent friction. Future investigations of other magnetic to nonmagnetic phase transformations will be necessary to determine if this new nonadiabatic picture is a general one for such materials.

[1] L. Delaey, in *Phase Transformations in Materials*, edited by R. W. Cahn, P. Hansen, and E. J. Kramer (VCH, Weinheim, Germany, 1991), pp. 583–654.
[2] R. A. Marcus, J. Chem. Phys. **24**, 966 (1956).
[3] P. M. Giles, M. Logenbach, and A. R. Marder, J. Appl. Phys. **42**, 4290 (1971).
[4] H. G. Bowden and P. M. Kelly, Acta Metall. **15**, 1489 (1967).
[5] D. Rittel, G. Ravichandran, and A. Venkert, Mater. Sci. Eng., A **432**, 191 (2006).
[6] J. M. Walsh, Bull. Am. Phys. Soc. **29**, 28 (1954).
[7] D. Bancroft, E. L. Peterson, and S. Minshall, J. Appl. Phys. **27**, 291 (1956).
[8] W. A. Bassett and E. Huang, Science **238**, 780 (1987).
[9] J. P. Rueff, M. Krisch, Y. Q. Cai, A. Kaprolat, M. Hanfland, M. Lorenzen, C. Masciovecchio, R. Verbeni, and F. Sette, Phys. Rev. B **60**, 14510 (1999).
[10] N. Von Bargen and R. Boehler, High Press. Res. **6**, 133 (1990).
[11] G. B. Olson and W. S. Owen, *Martensite* (ASM International, Materials Park, OH, 1992).
[12] K. J. Caspersen, A. Lew, M. Ortiz, and E. A. Carter, Phys. Rev. Lett. **93**, 115501 (2004).
[13] A. Lew, K. Caspersen, E. A. Carter, and M. Ortiz, J. Mech. Phys. Solids **54**, 1276 (2006).
[14] W. G. Burgers, Physica (Amsterdam) **1**, 561 (1934).
[15] H. K. Mao, W. A. Bassett, and T. Takahash, J. Appl. Phys. **38**, 272 (1967).

[16] F. M. Wang and R. Ingalls, Phys. Rev. B **57**, 5647 (1998).

[17] O. Mathon, F. Baudelet, J. P. Itie, A. Polian, M. d'Astuto, J. C. Chervin, and S. Pascarelli, Phys. Rev. Lett. **93**, 255503 (2004).

[18] F. Baudelet, S. Pascarelli, O. Mathon, J. P. Itie, A. Polian, M. d'Astuto, and J. C. Chervin, J. Phys.: Condens. Matter **17**, S957 (2005).

[19] D. H. Kalantar, J. F. Belak, G. W. Collins, J. D. Colvin, H. M. Davies, J. H. Eggert, T. C. Germann, J. Hawreliak, B. L. Holian, K. Kadau, P. S. Lomdahl, H. E. Lorenzana, M. A. Meyers, K. Rosolankova, M. S. Schneider, J. Sheppard, J. S. Stolken, and J. S. Wark, Phys. Rev. Lett. **95**, 075502 (2005).

[20] M. S. Grinolds, V. A. Lobastov, J. Weissenrieder, and A. H. Zewail, Proc. Natl. Acad. Sci. U.S.A. **103**, 18427 (2006).

[21] K. Kadau, T. C. Germann, P. S. Lomdahl, and B. L. Holian, Science **296**, 1681 (2002).

[22] K. Kadau, T. C. Germann, P. S. Lomdahl, R. C. Albers, J. S. Wark, A. Higginbotham, and B. L. Holian, Phys. Rev. Lett. **98**, 135701 (2007).

[23] R. E. Cohen, L. Stixrude, and E. Wasserman, Phys. Rev. B **56**, 8575 (1997).

[24] L. Stixrude, R. E. Cohen, and D. J. Singh, Phys. Rev. B **50**, 6442 (1994).

[25] P. Soderlind, J. A. Moriarty, and J. M. Wills, Phys. Rev. B **53**, 14063 (1996).

[26] E. G. Moroni and T. Jarlborg, Europhys. Lett. **33**, 223 (1996).

[27] L. Vocadlo, G. A. de Wijs, G. Kresse, M. Gillan, and G. D. Price, Faraday Discuss. 205 (1997).

[28] H. C. Herper, E. Hoffmann, and P. Entel, Phys. Rev. B **60**, 3839 (1999).

[29] M. Ekman, B. Sadigh, K. Einarsdotter, and P. Blaha, Phys. Rev. B **58**, 5296 (1998).

[30] H. Jónsson, G. Mills, and K. W. Jacobsen, in *Classical and Quantum Dynamics in Condensed Phase Simulations*, edited by B. J. Berne, G. Ciccotti, and D. F. Coker (World Scientific, Singapore, 1998), p. 385.

[31] M. Parrinello and A. Rahman, J. Appl. Phys. **52**, 7182 (1981).

[32] R. M. Wentzcovitch, Phys. Rev. B **44**, 2358 (1991).

[33] A. Laio and M. Parrinello, Proc. Natl. Acad. Sci. U.S.A. **99**, 12562 (2002).

[34] G. Henkelman, B. P. Uberuaga, and H. Jónsson, J. Chem. Phys. **113**, 9901 (2000).

[35] D. R. Trinkle, R. G. Hennig, S. G. Srinivasan, D. M. Hatch, M. D. Jones, H. T. Stokes, R. C. Albers, and J. W. Wilkins, Phys. Rev. Lett. **91**, 025701 (2003).

[36] K. J. Caspersen and E. A. Carter, Proc. Natl. Acad. Sci. U.S.A. **102**, 6738 (2005).

[37] G. Kresse and J. Furthmuller, Phys. Rev. B **54**, 11169 (1996).

[38] J. P. Perdew, K. Burke, and M. Ernzerhof, Phys. Rev. Lett. **77**, 3865 (1996).

[39] P. E. Blochl, Phys. Rev. B **50**, 17953 (1994).

[40] G. Kresse and D. Joubert, Phys. Rev. B **59**, 1758 (1999).

[41] D. E. Jiang and E. A. Carter, Phys. Rev. B **67**, 214103 (2003).

[42] E. G. Moroni, G. Kresse, J. Hafner, and J. Furthmuller, Phys. Rev. B **56**, 15629 (1997).

[43] V. Cocula, C. J. Pickard, and E. A. Carter, J. Chem. Phys. **123**, 214101 (2005).

[44] M. Methfessel and A. T. Paxton, Phys. Rev. B **40**, 3616 (1989).

[45] G. Steinle-Neumann, L. Stixrude, and R. E. Cohen, Phys. Rev. B **60**, 791 (1999).

[46] G. Steinle-Neumann, L. Stixrude, and R. E. Cohen, Proc. Natl. Acad. Sci. U.S.A. **101**, 33 (2004).

[47] G. Cort, R. D. Taylor, and J. O. Willis, J. Appl. Phys. **53**, 2064 (1982).

[48] S. Nasu, T. Sasaki, T. Kawakami, T. Tsutsui, and S. Endo, J. Phys.: Condens. Matter **14**, 11167 (2002).

[49] S. Merkel, A. F. Goncharov, H. K. Mao, P. Gillet, and R. J. Hemley, Science **288**, 1626 (2000).

[50] K. Shimizu, T. Kimura, S. Furomoto, K. Takeda, K. Kontani, Y. Onuki, and K. Amaya, Nature (London) **412**, 316 (2001).

[51] D. Jaccard, A. T. Holmes, G. Behr, Y. Inada, and Y. Onuki, Phys. Lett. A **299**, 282 (2002).

[52] E. Huang, W. A. Bassett, and P. L. Tao, J. Geophys. Res., [Solid Earth Planets] **92**, 8129 (1987).

[53] P. W. Anderson and E. I. Blount, Phys. Rev. Lett. **14**, 217 (1965).

[54] K. Nakamura and W. Kinase, J. Phys. Soc. Jpn. **61**, 2114 (1992).

[55] E. A. Carter and J. T. Hynes, J. Phys. Chem. **93**, 2184 (1989).

[56] J. T. Hynes, E. A. Carter, G. Ciccotti, H. J. Kim, D. A. Zichi, M. Ferrario, and R. Kapral, in *Perspectives in Photosynthesis*, edited by J. Jortner and B. Pullman (Kluwer, Netherlands, 1990), pp. 133–148.

[57] E. A. Carter and J. T. Hynes, J. Chem. Phys. **94**, 5961 (1991).